Front. Struct. Civ. Eng. 2022, 16(8): 962–975
https://doi.org/10.1007/s11709-022-0873-6

RESEARCH ARTICLE

Seismic responses and resilience of novel SMA-based self-centring eccentrically braced frames under near-fault ground motions

Zhi-Peng CHEN, Songye ZHU*

Department of Civil and Environmental Engineering, The Hong Kong Polytechnic University, Hong Kong 999077, China
**Corresponding author. E-mail: songye.zhu@polyu.edu.hk*

ABSTRACT In this paper, the seismic responses and resilience of a novel K-type superelastic shape memory alloy (SMA) self-centring (SC) eccentrically braced frame (EBF) are investigated. The simulation models of the SMA-based SC-EBF and a corresponding equal-stiffness traditional EBF counterpart are first established based on some existing tests. Then twenty-four near-fault ground motions are used to examine the seismic responses of both EBFs under design basis earthquake (DBE) and maximum considered earthquake (MCE) levels. Structural fragility and loss analyses are subsequently conducted through incremental dynamic analyses (IDA), and the resilience of the two EBFs are eventually estimated. The resilience assessment basically follows the framework proposed by Federal Emergency and Management Agency (FEMA) with the additional consideration of the maximum residual inter-storey drift ratio (MRIDR). The novel SMA-based SC-EBF shows a much better resilience in the study and represents a promising attractive alternative for future applications.

KEYWORDS shape memory alloy, eccentrically braced frame, self-centring, fragility, loss function, resilience

1 Introduction

Post-seismic repairable structures have drawn considerable attention from the earthquake engineering community over recent years. Consequently, increasing research interests have focused on the influence of permanent structural deformations, in addition to maximum transient deformation [1]. Eccentrically braced frames (EBFs) are a commonly accepted structural system in anti-seismic designs, and their structural responses and design approaches have been studied theoretically and experimentally [2,3]. Traditional EBF designs mainly focus on energy dissipation capacity achieved by a plump hysteresis behavior [3,4]. However, residual drifts associated with traditional EBFs may cause technical challenges in structural repair. For example, a 0.5% maximum residual inter-storey drift ratio (MRIDR) may result, finally, in the demolition of structures. Therefore, many recent studies have focused on self-centering (SC) EBF structures that exhibit limited post-seismic residual deformation [5,6].

Many SC devices and structural systems have been proposed in the past few decades. SC structures can recover most of the structural deformation, and provide a flag-shaped hysteresis performance that achieves a good balance between energy dissipation and low residual deformation. Among various realization techniques, post-tensioned (PT) tendons and cables are a predominant choice in SC devices and structures [7]. Although the efficiency of these PT-based structures has been demonstrated in past numerical and experimental studies and in real applications, several concerns have also been raised. The functionality of the PT-based structures is realized in the elastic range of the PT elements, and excessive structural deformations may cause functional loss [8]. Furthermore, the PT scheme plus extra energy dissipation devices lead to more complicated constructions and designs of structures compared with traditional structural systems.

In light of this, a novel shape memory alloy (SMA)

Article history: Received Jan 10, 2022; Accepted Jun 13, 2022

based SC-EBF, which is mainly constructed by using SMA angles and steel angles, is investigated in this study. Connected to link and collector beams through bolts, SMA angles can provide a good SC capacity and a moderate energy dissipation capacity due to their unique superelastic property. By using SMA-angles as the SC elements, the corresponding structural configuration can be greatly simplified, and its easy installation will benefit post-seismic repair and replacement.

In this paper, the seismic responses and resilience of the novel SMA-based SC-EBF are analyzed under near-fault ground motions and compared with a traditional EBF counterpart. Twenty-four existing near-fault ground motions are selected from database, and the corresponding structural performances under design basis earthquake (DBE) and maximum considered earthquake (MCE) are obtained. Structural fragility and loss analyses are conducted subsequently, and the resilience functions are eventually computed. Following a classical resilience analysis framework, the structural and non-structural losses caused by structural deformation and floor acceleration are considered. Furthermore, the effect of residual deformation on repairability is also considered to better reflect the monetary loss related to the structures. Compared with another study [9] that introduced the conceptual design, hysteresis behaviour and quasi-static cyclic behaviour of the SC-EBF, this paper focuses on the structural seismic performance levels with respect to structural repairability, adaptation, and resistance to seismic hazards. In doing so it considers the residual deformation effect using the emerging resilience framework.

2 Novel shape memory alloy based self-centering eccentrically braced frame

This section briefly introduces the material properties of SMA, the configuration of the novel SMA-based SC-EBF, and the establishment of the finite element models (FEMs).

2.1 Superelastic shape memory alloy

SMA is a novel high-performance structural material which has drawn much attention in recent years [10]. SMA exhibits two unique behaviours, namely, shape memory effect (SME) and superelasticity [11]. The former refers to the recovery of residual deformation induced by heating when the ambient temperature is lower than the martensite finish temperature. The latter describes the stress-induced recovery behaviour. When the ambient temperature is higher than the austenite finish temperature, the deformation of SMA elements can be fully recovered upon unloading. Superelastic SMA has been widely studied in the civil engineering field as an attractive SC element because of its typical flag-shaped hysteresis behaviour.

2.2 Configuration of shape memory alloy based self-centering eccentrically braced frame

Generally, several different types of EBFs can be found in the existing research and applications [12]. Different EBFs may have different design configurations, but their primary design objective is to concentrate plasticity development in the link beams in order to protect other parts of a structure from signficant damage or failure [13,14]. In this paper, a commonly used K-type EBF is chosen as an example. Figure 1 shows the construction of the novel K-type SMA-based SC-EBF. The major configuration, including the columns, collector beams, braces, and link beams, is similar to that of a traditional EBF. Stiffeners are also used to prevent local buckling. The main difference between the novel SMA-based SC-EBF and a traditional EBF is using the SMA and steel angle connections to replace the welding connections, changing the unrecoverable shear energy dissipation behaviour to recoverable centring-rocking behaviour. The hysteresis behaviour of the SMA-based SC-EBF is also changed from a plump loop with a large residual deformation to a flag shape with limited residual deformation. In post-seismic repair, the SC SMA angles can limit the residual inter-storey drift of the entire EBF in a repairable range (0.5% or less) [15], and the plastic development and failure are mainly concentrated in the easily-assembled steel angles. Consequently, a simple replacement can recover the structural function to a desirable level.

2.3 Finite element model establishment

The FEMs of the SMA-based SC-EBF and the corresponding traditional EBF with equivalent stiffness are established in the OpenSees software and then verified through several experimental tests. The model establishment approaches are shown in Fig. 2. The main parts of both EBFs are modelled by fibre beam and column elements, which have been proven to be efficient and accurate in previous studies [16,17]. The main difference between the two EBFs is the simulation of the link beams. In the SMA-based SC-EBFs (shown in Fig. 2(a)), the link beams exhibit the centring-rocking behaviour, and the gap opening and closing can activate the SMA and steel angles installed at the top and bottom flanges of the link beams. Therefore, an equal degree-of-freedom (DOF) connection is used to restrain the translation DOFs of the link beams and collector beams, while their rotation DOF is released. The SMA and steel angles are modelled by pairs of parallel springs, which are connected by rigid beam elements with a length equal to

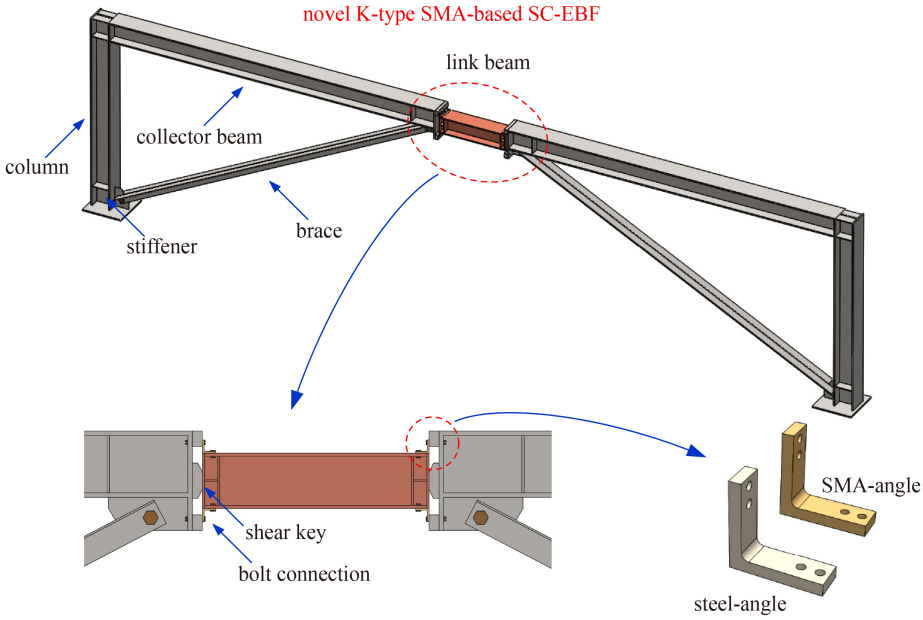

Fig. 1 The construction of the novel K-type SMA-based SC-EBF.

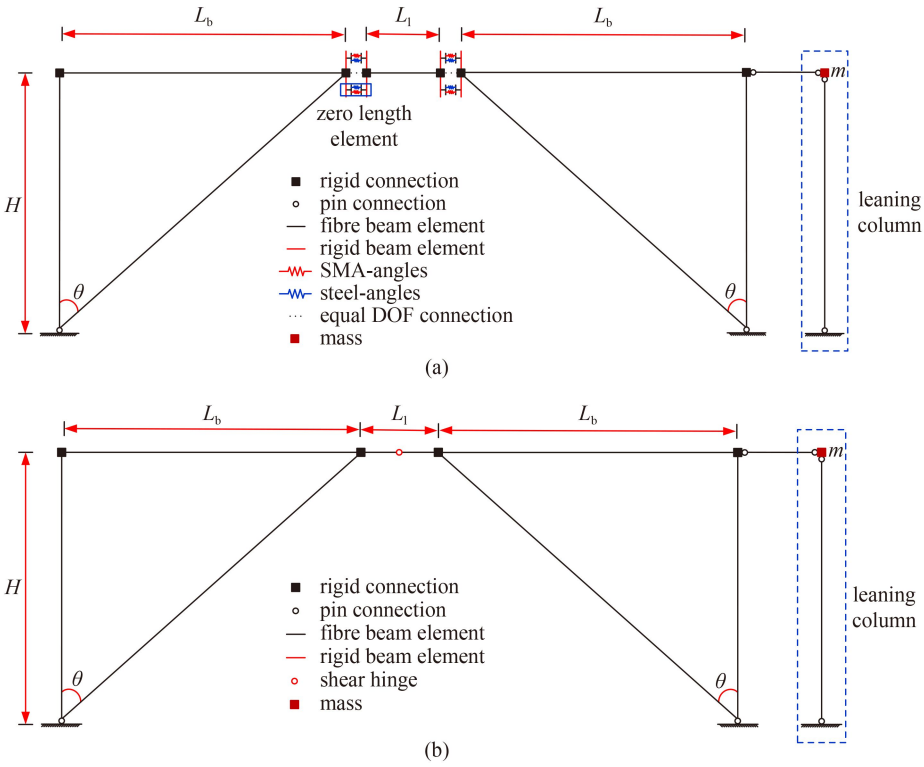

Fig. 2 FEM establishment of the EBFs. (a) Novel SMA-based SC-EBF; (b) traditional EBF.

the height of the link beam to simulate the rocking behaviour. In the traditional EBF model, the link beams and collector beams are rigidly connected to simulate the welding connections, and a shear hinge is added to reflect the shear behaviour when subjected lateral loads. Apart from the main elements, leaning columns are used to carry extra masses provided by other elements from the same floor [18], and the pin connection at the bottom can guarantee no extra lateral stiffness will be added by the leaning columns. Both EBFs are designed with pin foundations by following a common suggestion.

Because there is no testing result of the entire SMA-based EBF, a hybrid approach is used to validate the modelling of the individual components. Figure 3 compares the simulation of a traditional EBF with a tubular link beam reinforced by steel plates with the experimental

results obtained by Berman and Bruneau [19]. Figure 4 compares the simulation of the asymmetric behaviour of the steel angles, using the Steel4 material in OpenSees, with the previous test conducted by Wang and Zhu [20]. The key hysteresis parameters of the SMA angles are determined on the basis of the testing results by Wang and Zhu [21]. In addition, a sophisticated FEM of the SMA-based SC-EBF was established in Abaqus, and its accuracy has been demonstrated in the previous study [9]. As shown in Fig. 5(b), the simplified OpenSees model shows a good agreement with the simulation result of the sophisticated FEM. The comparisons in Figs. 3–5 demonstrate the efficacy and accuracy of the models of the two EBFs.

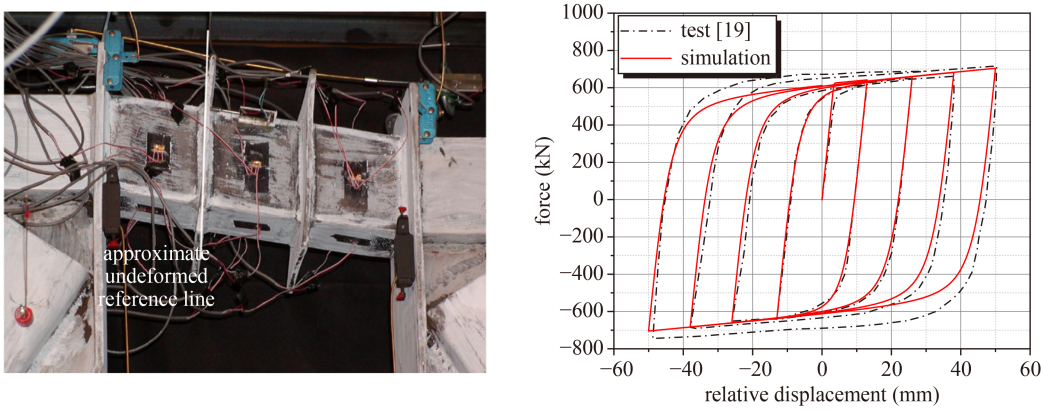

(a) (b)

Fig. 3 Model verification of traditional EBF. (a) Traditional EBF test [19]; (b) comparison between test and simulation of traditional EBF.

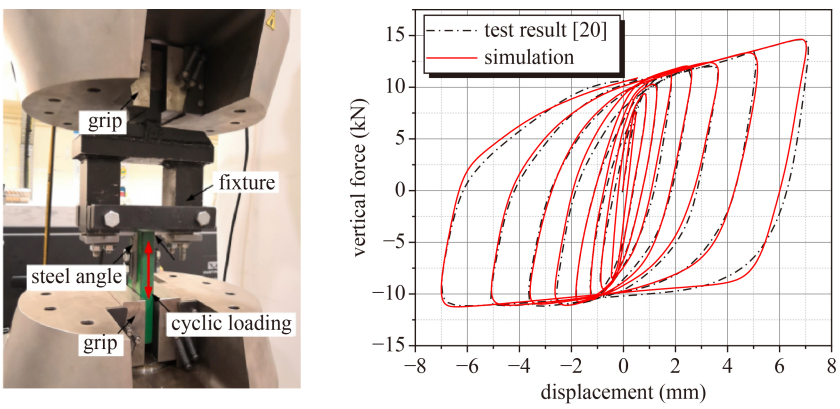

(a) (b)

Fig. 4 Model verification of the steel angles. (a) Test setup [20]; (b) Steel4 material model for steel angles.

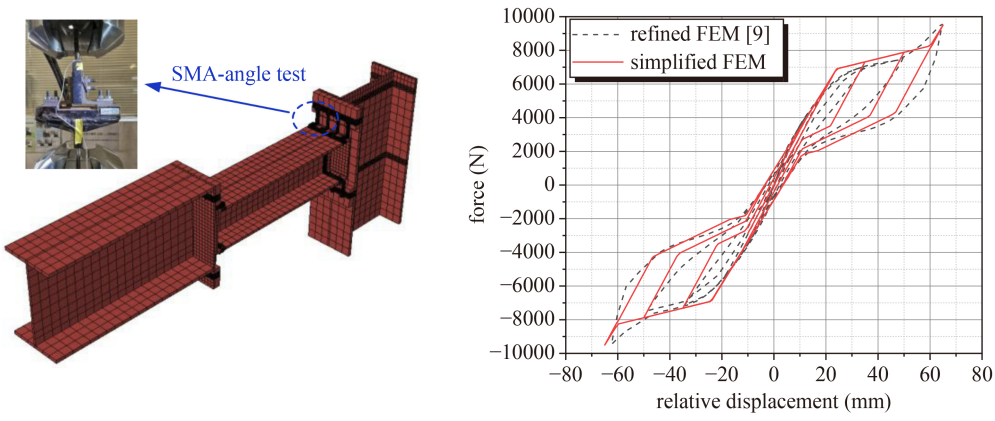

(a) (b)

Fig. 5 Model verification of SMA-based SC-EBF: (a) SMA-angle test and refined FEM of SMA-based SC-EBF [9]; (b) comparison of refined and simplified models of SMA-based SC-EBF.

3 Prototype building and seismic records

3.1 Prototype building

A prototype building designed for San Francisco, United States [8] is selected in this study for seismic performance assessment. The typical floor plan and the elevation layout are shown in Fig. 6. The dead load of the structure is 5 kN/m^2, and the live load is 2 kN/m^2 (but only half of the live load is considered in the following seismic analyses). The design of the traditional EBF follows AISC341-16/ASCE7-16. Subsequently, the link beam is replaced by an equal-elastic-stiffness SMA-based link beam to conduct a comparative study. Both EBFs are pin-connected to the base, and only one bay FEM of the braced frame is selected and established in the following analyses based on the approach mentioned in Section 2. The detailed design information is shown in Table 1. The fundamental periods of the traditional EBF and SMA-based SC-EBF are 2.28 and 2.29 s, respectively. Their fundamental periods are very close to each other, but their hysteresis behaviours are quite different, as shown in Fig 7.

3.2 Near-fault seismic records

Seismic hazards have long been a major concern for civil engineering structures. The effect of near-fault pulse-like ground motions has aroused great interest in recent decades. The early studies on near-fault earthquakes date back to 1978, when Bertero et al. [22] pointed out that long-period pulse shaking was the main reason causing the damage of a hospital building in the San Fernando earthquake (1971). The concept of near-fault was firstly proposed by Bolt [23], and now this term is used to describe the regions where the site-to-source is less than 20 km. Somerville et al. [24] confirmed that the long-period velocity pulses can cause forward-directivity (FD) effect and fling-step (FS) effect, in which the sudden seismic energy input is extremely high, causing severe global and local failures. Therefore, many studies have been conducted to discuss the near-fault seismic responses of structures, and the corresponding results have indicated that the near-fault earthquakes may cause unexpected damage to structures, and special attention should be paid to them [25,26]. Considering this, the near-fault seismic records are chosen in this study to investigate the effectiveness of the novel SMA-based SC-EBF.

In this study, data from twenty-four near-fault seismic records containing FD effect, FS effect, and non-pulse are selected to consider the uncertainty in earthquakes [27,28]. All the records are selected from the Pacific Earthquake Engineering Research Center (PEER) database, and are then scaled to match the DBE and MCE spectra of an intensity level of 7 defined in Chinese code GB50011 [29], wherein the DBE and MCE correspond to the returning periods of 475 and 2475 years. Detailed information of all the selected seismic records is shown in Table 2, and the scaled spectra for DBE are shown in Fig. 8. In general, the median spectrum of the scaled

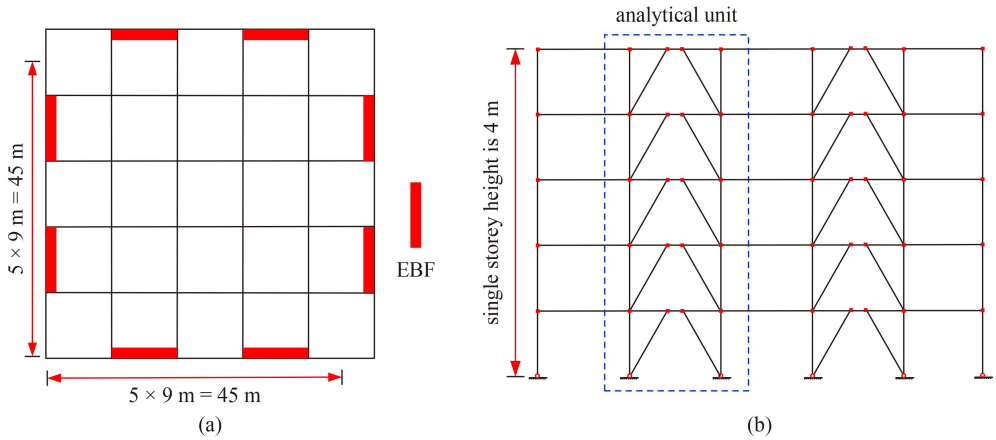

Fig. 6 The prototype structure. (a) Typical floor plan; (b) elevation layout.

Table 1 The designs of the prototype structures

structure type	storey No.	column	beam	bracing	link beam	angles*	material
traditional EBF	1–3	W14 × 132	W14 × 48	W8 × 40	W10 × 49	–	A992 steel
	4–5	W14 × 68	W14 × 43	W8 × 31	W10 × 45	–	A992 steel
SMA-based SC-EBF	1–3	W14 × 132	W14 × 48	W8 × 40	W10 × 49	100 × 50 × 100	A992 steel
	4–5	W14 × 68	W14 × 43	W8 × 31	W10 × 45	80 × 50 × 100	A992 steel

*Note: The angles are designed with equal length of both legs. Their dimension are presented as the leg width × leg thickness × leg length (unit: mm).

seismic records shows a good agreement with the target spectrum in the interested period range of 0.5–4 s that covers the majority of structural periods. This agreement shows that the selected set of the near-fault seismic records can accurately reflect the expected seismic intensity level.

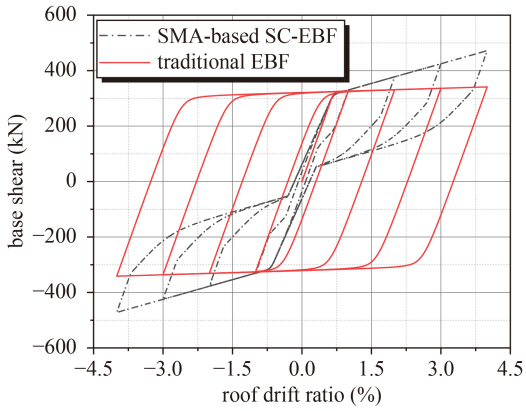

Fig. 7 The cyclic pushover behaviours of the two EBFs.

4 Seismic performance assessment

4.1 Time-history analyses in the target intensity levels

The seismic performances of the two EBFs are firstly investigated under the DBE and MCE levels that correspond to the return periods of 475 and 2475 years, respectively [29]. The seismic performances are assessed with respect to three different indexes, namely, maximum inter-storey drift ratio (MIDR), MRIDR, and peak floor acceleration (PFA). These three indexes are widely accepted to reflect the damage and loss of structural and non-structural elements [30].

The MIDRs of the two EBFs are shown in Fig. 9. The "SMA" in the legend corresponds to the novel SMA-based SC-EBF, while the "traditional" refers to the traditional EBF. As shown in Fig. 9, both EBFs show similar heightwise profiles, in which the MIDRs of the EBFs appear in the first storey. The MIDRs generally decrease as the floor height increases except for the forth storey, where the beam and column section size reduces. Both EBFs show a typical shear-type deformation under

Table 2 Detailed information of the selected seismic records

records type	No.	earthquake	station	magnitude	scale factor
FD seismic records	1	Northridge	Jensen Filter Plant Administrative Building	6.69	0.1116
	2	Northridge	Rinaldi Receiving Sta	6.69	0.0923
	3	Northridge	Sylmar-Converter Sta	6.69	0.0825
	4	Northridge	Sylmar-Converter Sta East	6.69	0.1095
	5	Northridge	Sylmar-Olive View Med FF	6.69	0.1412
	6	Chi-Chi	TCU051	7.62	0.3347
	7	Chi-Chi	TCU082	7.62	0.2823
	8	Chi-Chi	TCU102	7.62	0.1338
FS seismic records	9	Kocaeli	Yarimca	7.51	0.1818
	10	Chi-Chi	TCU026	7.62	0.5122
	11	Chi-Chi	TCU052	7.62	0.103
	12	Chi-Chi	TCU065	7.62	0.1004
	13	Chi-Chi	TCU068	7.62	0.0946
	14	Chi-Chi	TCU075	7.62	0.1831
	15	Chi-Chi	TCU076	7.62	0.2605
	16	Chi-Chi	TCU087	7.62	0.4141
Non-pulse seismic records	17	Northridge	Arleta-Nordhoff Fire Sta	6.69	0.3117
	18	Northridge	Northridge-17645 Saticoy St	6.69	0.2829
	19	Northridge	Simi Valley-Katherine Rd	6.69	0.2666
	20	Northridge	Tarzana-Cedar Hill A	6.69	0.1351
	21	Kobe	Nishi-Akashi	6.9	0.2955
	22	Chi-Chi	TCU071	7.62	0.1772
	23	Chi-Chi	TCU072	7.62	0.1658
	24	Chi-Chi	TCU078	7.62	0.2576

lateral loads, which is consistent with the design target. The MIDRs of novel SMA-based SC-EBF are larger than those of the traditional EBF by about 15% and 8% under the DBE and MCE levels, respectively. This phenomenon is caused by the relatively lower energy dissipation capacity of the SMA-based SC-EBF, which is an inherent characteristic of the flag-shaped hysteresis curves of typical SC structures. Therefore, when designed with the same elastic stiffness and yield strength, the MIDR of the SMA-based SC-EBF will be slightly larger than that of traditional EBFs. However, both EBFs are in the range of the limit value recommended by FEMA 356, indicating that the MIDR of the SMA-based SC-EBF is acceptable.

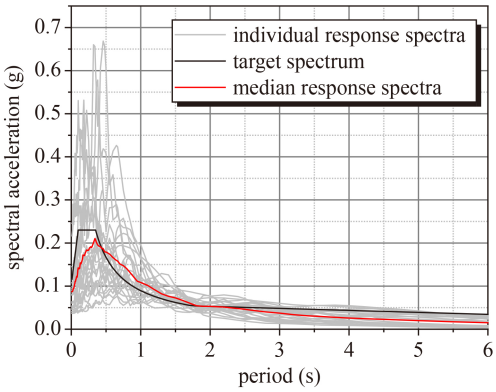

Fig. 8 The DBE spectra of the selected seismic records.

The SC capacity of the EBFs is mainly reflected by the MRIDR at two intensity levels, as shown in Fig. 10. Unlike the behavior illustrated in Fig. 9, in which the two EBFs exhibit similar MIDR performance at both intensity levels, the MRIDR performances of the two structures are considerably different at the MCE level. Figure 10(a) shows that the MRIDRs of the SMA-based SC-EBF and the traditional EBF are still similar at a DBE level. The median value of the traditional EBF is slightly larger, but it is still in the range of the repairable limit value of 0.5% because the major parts of the traditional EBF are still in an elastic range. The median MIDR in DBE is only around 0.8% (as shown in Fig. 9); as a result, the residual deformation can be controlled within an acceptable range. However, from examining the record-to-record variability it can be seen that the MRIDRs of two seismic records are far beyond the limit value, showing that the repairability of the traditional EBF cannot be fully guaranteed even at the DBE level. Figure 10(b) shows

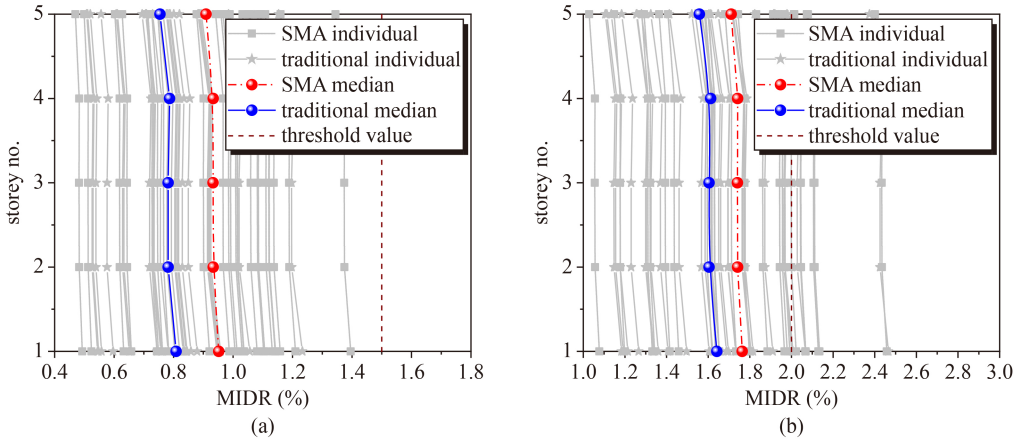

Fig. 9 The MIDR of the two EBFs. (a) DBE level; (b) MCE level.

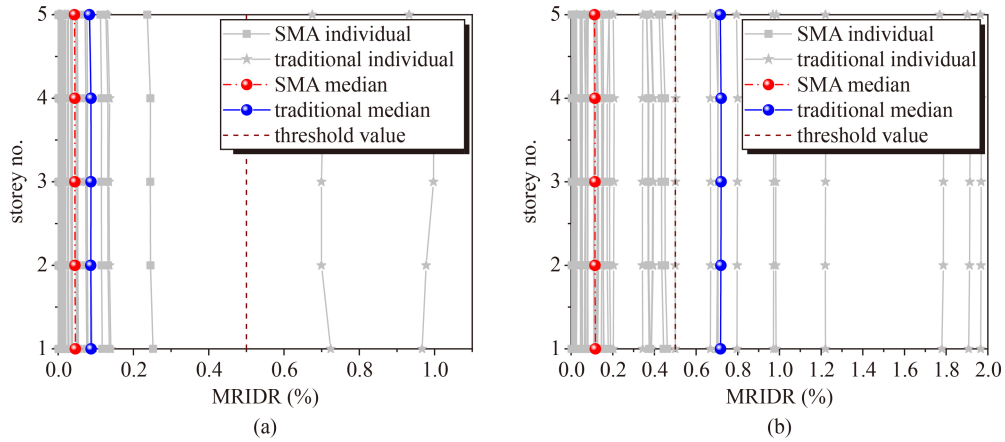

Fig. 10 The MRIDR of the two EBFs. (a) DBE level; (b) MCE level.

considerably different performances at the MCE level. The median MRIDR value of the traditional EBF exceeds the repairable limit value, and the MRIDR values relating to several earthquakes even reach four times the limit value. In comparison, the median MRIDR value of the SMA-based SC-EBF is only about 0.12%, reduced by about 80% compared with that of traditional EBF (around 0.72%).

Comparing both the MIDR and MRIDR of the two EBFs, the SMA-based SC-EBF sacrifices about 10% to 15% of MIDR performance; but it reduces the MRIDR by about 80%, guaranteeing that the entire EBF is repairable at both the DBE and MCE levels. Therefore, the overall seismic performances of the SMA-based SC-EBF are considered to be better.

Figure 11 shows the PFA of the two EBFs at the two different intensity levels. Unlike the MIDR and MRIDR, the PFAs are not sensitive to the structural forms. For DBE and MCE, the median values and the heightwise distribution of the PFAs are similar in the two EBFs, showing that different types of hysteresis behaviour have little impact on the PFAs in this case.

4.2 Seismic resilience assessment

Resilience is an emerging concept which combines adapting disturbance, mitigating hazards, and recovering a structure or a city after extreme seismic events. The seismic resilience-based structural performance assessment has attracted broad interest recently, with several typical frameworks proposed. Seismic resilience is adopted as an effective index to assess structural damage, recovery, and monetary loss related to a certain hazard. Therefore, seismic resilience is used in this section to evaluate the seismic behaviour of the two EBFs.

4.2.1 Resilience assessment considering residual deformation

The classical resilience assessment approach proposed by Bruneau et al. [31] and Cimellaro et al. [32] has been widely accepted. The structural resilience R can be expressed as

$$R = \int_{t_0}^{t_0+T_{\mathrm{LC}}} \frac{Q(t)}{T_{\mathrm{LC}}} \mathrm{d}t, \tag{1}$$

where $Q(t)$ is the structural function, and T_{LC} is the assessment period of the structural resilience.

The key objective in resilience assessment is to determine the structural function $Q(t)$ (shown in Fig. 12), which can be expressed as

$$Q(t) = 1 - \{L_{\mathrm{IM}} \times [H(t-t_0) - H(t-(t_0+T_{\mathrm{RE}}))] \times f_{\mathrm{re}}(t)\}, \tag{2}$$

where L_{IM} is the structural function loss at a certain intensity measure, $H(\cdot)$ is the Heaviside step function, and f_{re} is the recovery function and has several different forms [33]. In this paper, the recovery function is chosen as

$$f_{\mathrm{re}}(t) = 0.5 \times \{1 + \cos[\pi(t-t_0)/T_{\mathrm{RE}}]\}. \tag{3}$$

The allowable range of $Q(t)$ is from 0 to 100%, in which the lower and upper limits represent the structural conditions corresponding to the total collapse and without any damage, respectively.

In the previously mentioned framework, the loss function, which links the structural responses and structural function loss, is needed. In the current FEMA framework [34,35], the loss estimate model can be expressed as

$$L_{\mathrm{IM}} = \sum_{i}^{m} \sum_{j}^{n} \eta_{ij|\mathrm{IM}} P_{ij|\mathrm{IM}}, \tag{4}$$

where η is the damage ratio at a certain intensity measure, P is the corresponding exceedance ratio calculated by fragility analysis, m is the number of considered loss types, and n is the number of limit states in every loss type. In this study, the analysis framework generally

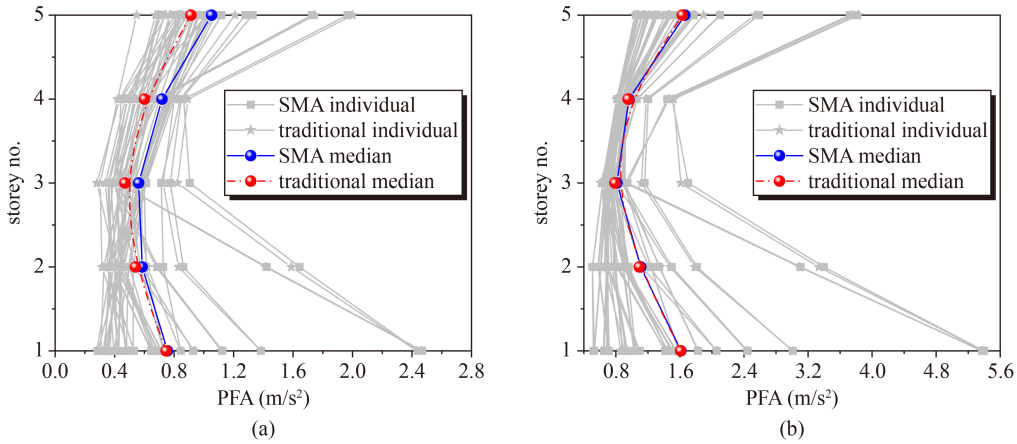

Fig. 11 The PFA of the two EBFs. (a) DBE level; (b) MCE level.

follows FEMA's recommendation [36], and three different loss types (m = 3), namly, structural loss induced by MIDR, non-structural loss induced by MIDR, and non-structural loss induced by PFA, are chosen. The damage ratios and limit states divisions are shown in Table 3. Four different limit states (n = 4) are considered, and j = 4 represents the collapse state while j = 1, 2, 3 represents slight, moderate, and extensive damage limit states, respectively. The corresponding damage ratios and limit states divisions are shown in Table 3.

In the original FEMA framework, the loss of a structure is categorized as collapse loss $L_{\mathrm{C|IM}}$ (j = 4) and repair loss $L_{\mathrm{R|IM}}$ (j = 1, 2, 3). However, in recent studies, researchers found that although some structures are free from collapse, the repair is so uneconomic and difficult that structural demolition is finally needed. The residual drift ratio of 0.5% is widely accepted as the threshold value that divides repair and demolition [15]. Therefore, the total loss of a structure in this paper is divided into three parts by following the suggestion by Xu et al. [36], namely, repairable (when MIDR is lower than the collapse limit state and MRIDR is lower than 0.5%), collapse (MIDR is higher than the collapse limit state), and demolition (MIDR is lower than the collapse limit state but MRIDR is higher than 0.5%). The loss function in this framework can be expressed as

$$L_{\mathrm{IM}} = L_{\mathrm{C|IM}} + L_{\mathrm{R|IM}} + L_{\mathrm{D|IM}}, \tag{5.1}$$

$$L_{\mathrm{C|IM}} = \sum_{i}^{m} \eta_{i,j=4|\mathrm{IM}} P_{i,j=4}, \tag{5.2}$$

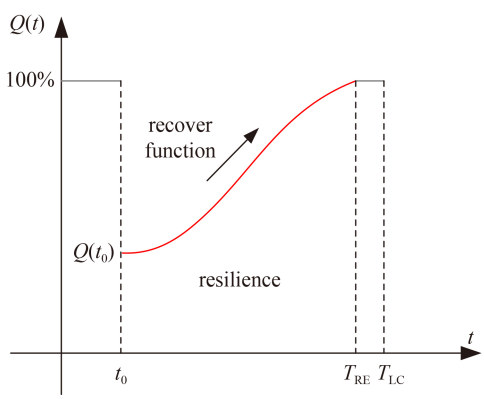

Fig. 12 Typical resilience function.

$$L_{\mathrm{R|IM}} = \sum_{i}^{m} \sum_{j=1}^{3} \eta_{ij|\mathrm{IM}} P_{ij|\mathrm{IM}} \cdot (1 - P_{\mathrm{D}|i,j,\mathrm{IM}}), \tag{5.3}$$

$$L_{\mathrm{D|IM}} = \sum_{i}^{m} \sum_{j=1}^{3} \eta_{i,j=4|\mathrm{IM}} P_{ij|\mathrm{IM}} \cdot P_{\mathrm{D}|i,j,\mathrm{IM}}, \tag{5.4}$$

where $P_{\mathrm{D}|ij,\mathrm{IM}}$ is the individual probability of exceedance of 0.5% MRIDR of each limit state in structural fragility analyses.

In this study, the analysis framework generally follows FEMA's recommendation, and three different loss types, namely, structural loss induced by MIDR, non-structural loss induced by MIDR, and non-structural loss induced by PFA, are chosen.

4.2.2 Fragility analysis

As mentioned in Subsubsection 4.2.1, the first step in the resilience analysis is to determine the probability of exceedance at a given seismic intensity measure (IM), which can be obtained through fragility analysis. A widely-adopted fragility analysis approach was proposed by Cornell et al. [37] and Chen et al. [38] who defined the probability of exceedance of a certain limit state at a given intensity level and can be expressed as

$$P[D > C] = \Phi\left[\frac{\ln(S_{\mathrm{d}}/S_{\mathrm{c}})}{\sqrt{\beta_{\mathrm{d}}^2 + \beta_{\mathrm{c}}^2}}\right], \tag{6}$$

where D and C stand for engineering demand parameters (EDPs) and structural capacity, respectively; S_{d} and S_{c} are the median value of structural demand and the median value of structural capacity, respectively; β_{d} and β_{c} are the uncertainty of structural demand and capacity, respectively; and $\Phi[\cdot]$ is the standard normal distribution function. The statistical data in fragility is usually obtained by incremental dynamic analysis (IDA). The median value and standard deviation obtained from the linear regression of the IM-EDP relationships can be used in Eq. (6) [39–41].

In this study, the seismic records shown in Table 2 are scaled and used in IDA, and then the calculated results are used in the fragility analysis. Because there are three different loss types considered in the resilience

Table 3 Damage ratios and threshold values of the four limit states

damage state	structural (i = 1)		drift-non-structural (i = 2)		acc.-non-structural (i = 3)	
	damage ratio η (%)	threshold value	damage ratio η (%)	threshold value	damage ratio η (%)	threshold value
slight (j = 1)	0.3	0.33% MIDR	0.7	0.4% MIDR	1	0.25g PFA
moderate (j = 2)	1.4	0.58% MIDR	3.4	0.8% MIDR	5.2	0.5g PFA
extensive (j = 3)	7.2	1.56% MIDR	17.2	2.5% MIDR	15.3	1.0g PFA
collapse (j = 4)	14.4	4.00% MIDR	34.4	5.00% MIDR	51.2	1.6g PFA

calculation, a unified IM should be chosen for all three analyses. Traditional IMs such as PGA, PGV, and SaT_1 may show some limitations in one or two types of loss calculations. Sa_{avg} is adopted as IM in this study according to the suggestions in Refs. [42,43]. This IM is also called average spectral acceleration and is defined as

$$Sa_{\text{avg}}(\zeta_1 T_1, \ldots, \zeta_n T_1) = \left(\prod_{i=1}^{n} Sa(\zeta_i T_1) \right)^{1/n}, \tag{7}$$

where n is the number of periods for calculating Sa_{avg}, and ζ_i is a non-dimensional parameter, ranging from 0.25 to 3 in this study. Following the probabilic seismic demand analysis (PSDA) in previous studies [42,43], in which the certain probabilistic relationship between the selected IM and EDP are calculated and assessed, the Sa_{avg} and selected EDPs (here are MIDR, MIRDR, and PFA) show a typical log-normal relationship and are suitable for the following fragility analysis.

The fragility analysis results of the three different loss types are shown in Fig. 13, and the results of MRIDR are shown in Fig. 14. The results of the fragility analysis show a similar trend to those described in Subsection 4.1. Compared with the traditional EBF, the SMA-based SC-EBF shows slightly worse control in drift performances, an obvious advantage in controlling residual drift performance, and a similar performance in PFA. One notable point is that Fig. 14(b) shows the probability of exceedance of MRIDR = 0.5%, which is the $P_{\text{D}|ij,\text{IM}}$ in Eq. (5). This probability of exceedance is defined as the ratio between the cases with MRIDR exceeding 0.5% to the number of cases in each individual limit state (i.e. slight, moderate, extensive, and collapse limit states). Only the $P_{\text{D}|ij,\text{IM}}$ in the slight, moderate and extensive limit states are presented in this figure, while the probability in the collapse state is not needed in Eq. (5.3). The $P_{\text{D}|ij,\text{IM}}$ for slight structural damage is zero, and it is not zero for slight drift-sensitive non-structural damage in the traditional EBF. From Fig. 14(b), the max $P_{\text{D}|ij,\text{IM}}$ of the traditional EBF is larger than those of SMA-based SC-EBF in all limit states. This indicates that the large residual deformation of the traditional EBF often makes the structure unrepairable in most moderate and extensive damage states, but for the SMA-based SC-EBF, the desirable SC capacity makes the structure repairable in most cases.

After determining the structural fragility curves, the structural loss function can be calculated using Eq. (5),

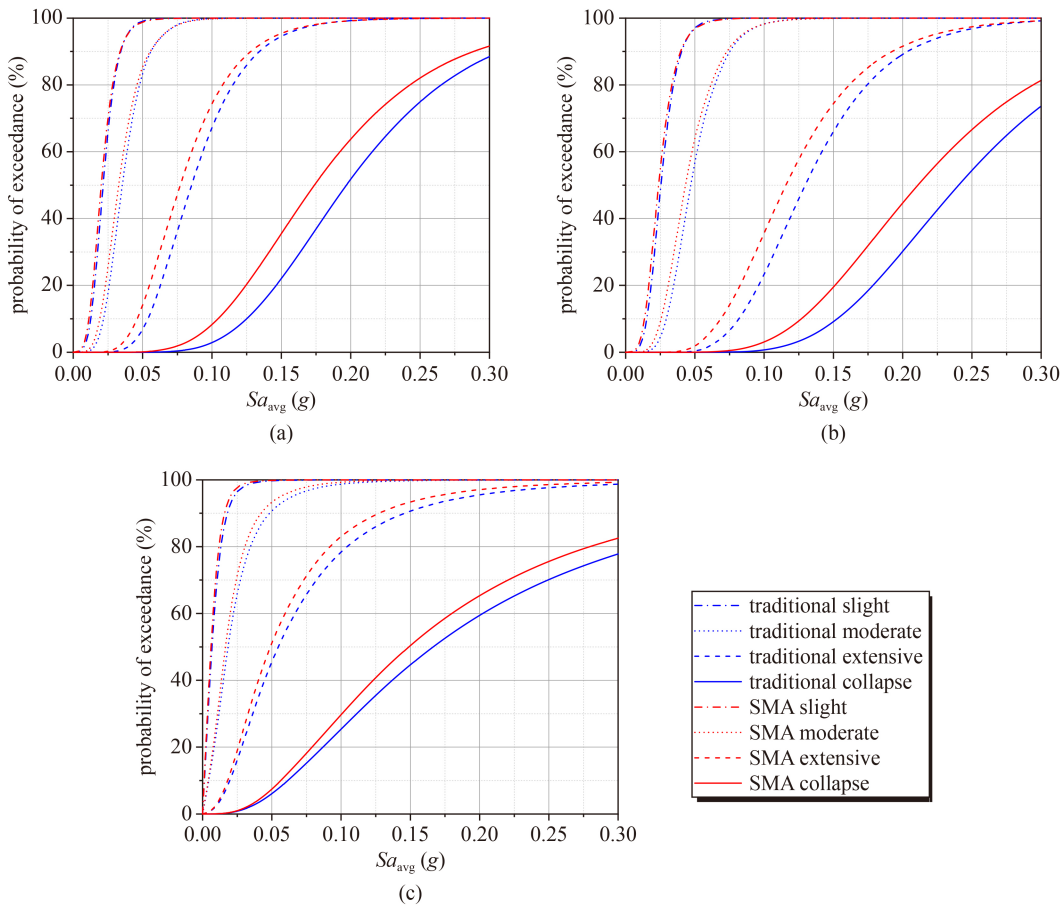

Fig. 13 The fragility curves of the three loss types. (a) Structural losses induced by MIDR; (b) non-structural losses induced by MIDR, (c) non-structural losses induced by PFA.

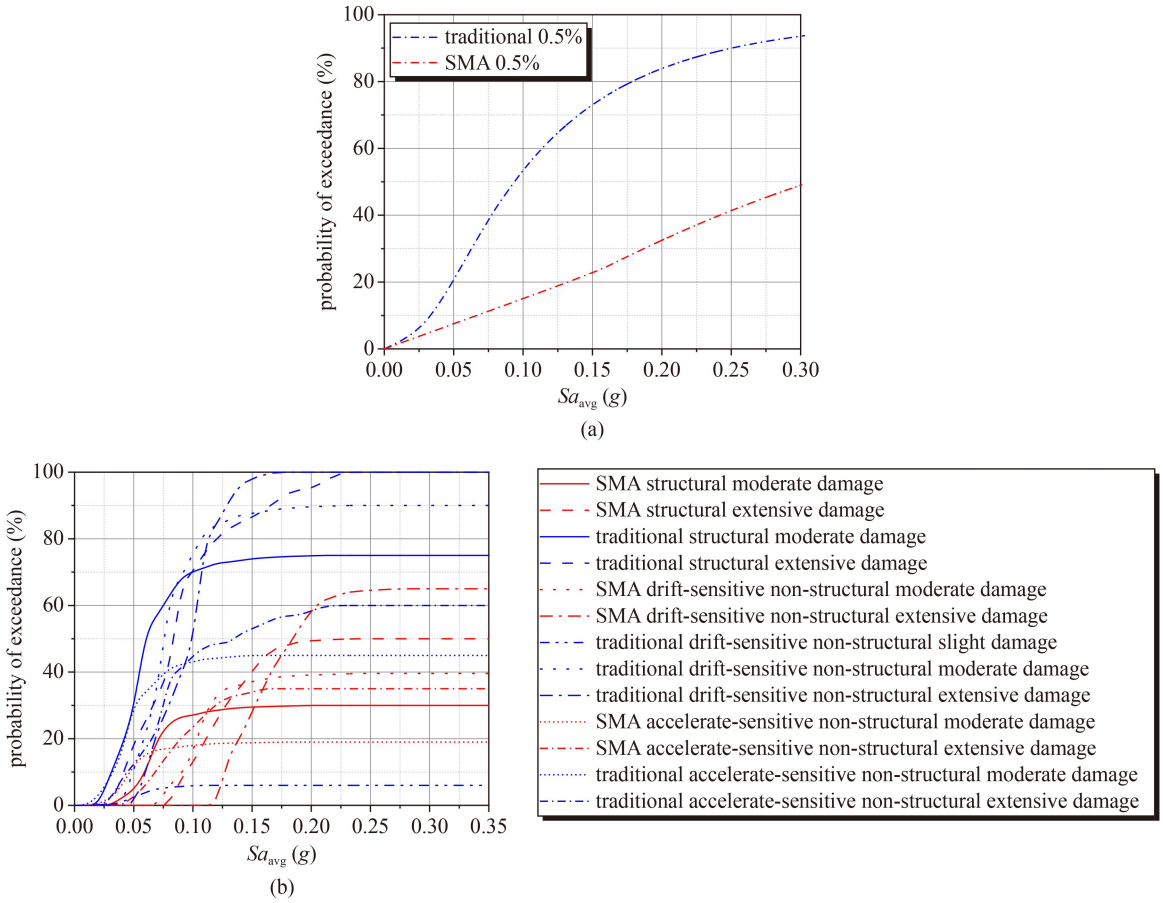

Fig. 14 The fragility curves of the MRIDR. (a) Entire MRIDR; (b) individual probability of exceedance of 0.5% MRIDR in each limit state.

and the results are shown in Figs. 15 and 16. Both EBFs have similar loss ratios at the end (nearly 100% at 0.35g Sa_{avg}), because their similar MIDRs lead to collapse at this extremely large IM. However, the loss ratio of the traditional EBF grows much faster between the DBE and MCE levels, which is mainly caused by the rapid increase in the demolition loss. In this range, the residual deformations of the traditional EBF grow rapidly, and mostly exceed the repairable limit value of 0.5% MRIDR at the MCE level. In contrast, the residual drift of the SMA-based SC-EBF is much smaller, and most damages are still repairable at this stage. Consequently, the demolition loss and the total loss of traditional EBF are considerably higher than those of SMA-based SC-EBF.

As shown in Fig. 16, the repair loss and collapse loss of the SMA-based SC-EBF are slightly greater than those of the traditional EBF at both the DBE and MCE levels. The former is caused by the good SC capacity of the SMA-based SC-EBF, which makes most damages repairable and thus contains more cases in this loss type. The latter is caused by the effect of less energy dissipation capacity of the SC-EBF on the MIDR. However, because the MIDR of the SC-EBF is only slightly larger than that of the traditional EBF, the increase in the collapse loss is actually minimal. The demolition loss of the traditional EBF at both the DBE and MCE levels is considerably greater than that of the SMA-based SC-EBF, resulting in a significant increase in the total loss of the traditional EBF. This phenomenon reflects that although the traditional EBF has some advantage in energy dissipation and peak drift control, its weakness in controlling residual drift causes significant monetary loss due to the unrecoverable residual deformation and the corresponding structural demolition loss.

4.2.3 Resilience

Based on the results and Eqs. (2) and (3), the resilience of the two EBFs at certain intensity levels can be calculated. The recovery days of both structures under no damage, slight damage, moderate damage, extensive damage, and collapse are chosen as 0, 10, 90, 270, 360 d. If the structural MRIDR exceeds 0.5%, the structure is regarded as ‘demolition’, and the recovery days are chosen to be the same as for collapse [33]. Considering the recovery days under the 24 earthquakes, the average recovery days of the traditional EBF are 103 and 255 d at the DBE and MCE levels, and for the SMA-based SC-EBF, the values are 87 and 240 d at the DBE and MCE levels. The

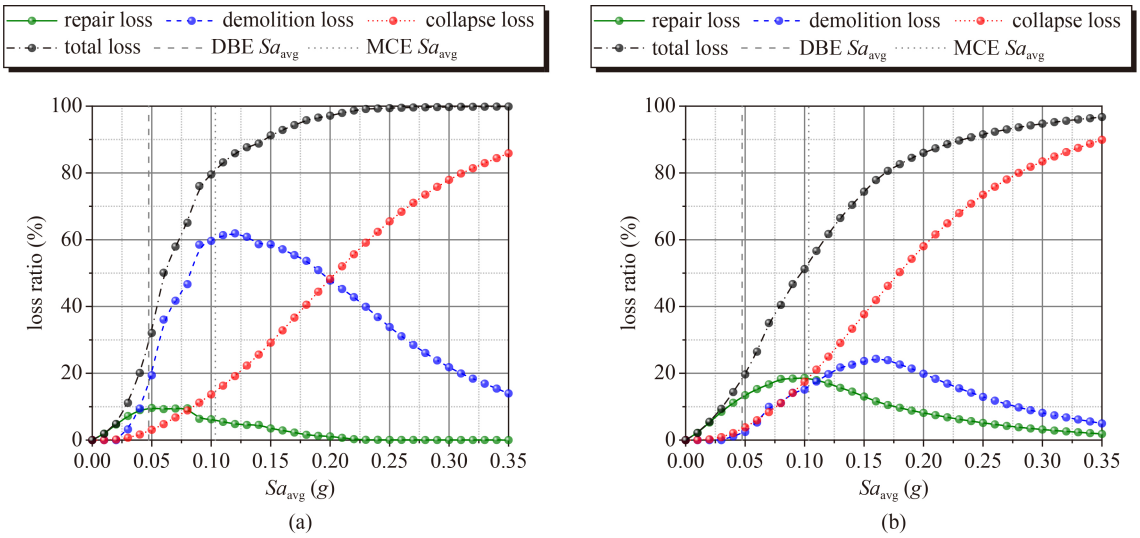

Fig. 15 The loss function of the two EBFs. (a) Traditional EBF; (b) SMA-based SC-EBF.

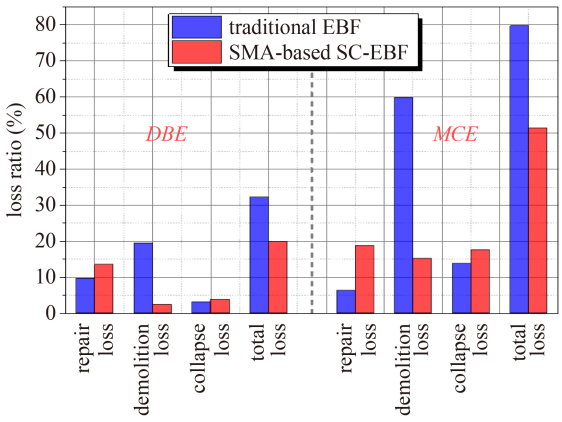

Fig. 16 The loss ratio of the two EBFs in DBE and MCE level.

SMA-based SC-EBF has a shorter recovery period in both DBE and MCE, showing that the SC capacity can increase the repairability of the structure. The resilience curves of these two structures are shown in Fig. 17. The structural function loss of the traditional EBF is more serious at the DBE and MCE levels, and the resilience is much worse. At the DBE level, the resilience is 0.88 and 0.94 for the traditional EBF and SMA-based SC-EBF, respectively; and the lowest structural function is 70.7% and 81.6% for the two EBFs, respectively. However, at the MCE level, the resilience of the traditional EBF drops to 0.646 and the lowest structural function drops to only 19.2%, less than half of that of the SMA-based SC-EBF (46.9%), which means the structural function is nearly lost completely in this limit state. This phenomenon is caused by the large residual deformation of the traditional EBF, causing a huge demolition loss. In the SMA-based SC-EBF, however, the desirable SC capacity guarantees that the damage at most intensity levels is repairable, limiting the structural loss within a much smaller range, and largely increasing the structural resilience under earthquakes. Considering all the previous discussions, the SMA-based SC-EBF is a promising novel structural system in earthquake engineering.

5 Conclusions

In this paper, the seismic performances and resilience of a novel SMA-based SC-EBF are investigated and compared with a traditional EBF with equivalent stiffness. The major conclusions of this study are summarized as follows.

1) Compared with the traditional EBF using the welding connection between the link and collector beams, the novel SMA-based SC-EBF uses SMA angles and bolt connections, and its simple configuration may considerably facilitate post-seismic replacement and repair.

2) In time–history analyses at both DBE and MCE, the SMA-based SC-EBF shows slightly worse control in MIDR than the traditional EBF, because of the inherently less energy dissipation of the flag-shaped hysteresis behaviour. However, the novel SMA-based SC-EBF shows an obvious advantage in terms of controlling MRIDR. Therefore, the SMA-based SC-EBF sacrifices only 10%–15% of MIDR performances, but reduces MRIDR by about 80%, which guarantees that the entire EBF is repairable at both the DBE and MCE levels. The PFAs of both EBFs are similar, showing that this response measure is not obviously influenced by the forms of the EBFs.

3) In the loss analysis, the SMA-based SC-EBF has slightly higher repair loss and collapse loss, but considerably lower demolition loss than the traditional EBF at both DBE and MCE. Consequently, the total loss of the novel SMA-based SC-EBF is significantly reduced. This observation reflects that although the traditional EBF has some advantage in energy dissipation and drift

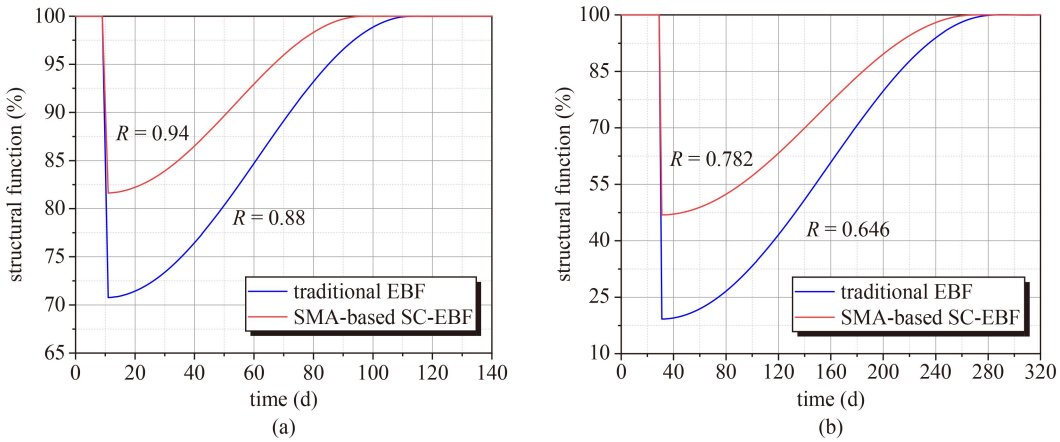

Fig. 17 Resilience of the two EBFs. (a) DBE level; (b) MCE level.

control, the weakness in controlling residual drift can cause significant monetary loss due to the unrecoverable residual deformation and the corresponding structural demolition loss.

4) The resilience analysis reveals that the SMA-based SC-EBF performs much better than the traditional EBF at both the DBE and MCE levels. The structural function of the traditional EBF is nearly lost completely at the MCE level, showing that the large MRIDR of the traditional EBF causes large demolition loss and eventually decrease the structural resilience considerably. Considering its overall performance, the SMA-based SC-EBF is regarded as a promising novel seismic-resistant structural system.

Acknowledgements The authors are grateful for the financial supports from the Research Grants Council of Hong Kong through the GRF Project (No. PolyU 152246/18E), the National Key Research and Development Program of China (No. 2019YFB1600700), and the Hong Kong Polytechnic University (Nos. ZE2L, ZVX6, and P0035787). The findings and opinions expressed in this paper are solely those of the authors and do not represent the view of the sponsors.

References

1. Wilson J C, Wesolowsky M J. Shape memory alloys for seismic response modification: A state-of-the-art review. Earthquake Spectra, 2005, 21(2): 569−601
2. Fujimoto M, Aoyagi T, Ukai K, Wada A, Saito K. Structural characteristics of eccentric K-braced frames. Journal of Environmental Engineering, 1972, 195: 39−49
3. Hjelmstad K D, Popov E P. Characteristics of eccentrically braced frames. Journal of Structural Engineering, 1984, 110(2): 340−353
4. Foutch F A. Seismic behavior of eccentrically braced steel building. Journal of Structural Engineering, 1989, 115(8): 1857−1876
5. Qiu C, Zhu S. Shake table test and numerical study of self-centering steel frame with SMA braces. Earthquake Engineering & Structural Dynamics, 2017, 46(1): 117−137
6. Deng K L, Pan P, Wu S J. Experimental study on a self-centering coupling beam eliminating the beam elongation effect. Structural Design of Tall and Special Buildings, 2016, 25(6): 265−277
7. Tong L, Zhang Y, Zhou X, Keivan A, Li R. Experimental and analytical investigation of D-type self-centering steel eccentrically braced frames with replaceable hysteretic damping devices. Journal of Structural Engineering, 2019, 145(1): 04018229
8. Aied Qissab Al-Janabi M, Yang T Y. Seismic performance assessment of novel self-centering friction-based eccentrically braced frames. Engineering Structures, 2021, 241: 112456
9. Chen Z P, Zhu S, Yu H, Wang B. Development of novel SMA-based D-type self-centering eccentrically braced frames. Engineering Structures, 2022, 260: 114228
10. Wang B, Zhu S Y, Jiang H J. Earthquake resilient RC walls using shape memory alloy bars and replaceable energy dissipating devices. Smart Materials and Structures, 2019, 28(6): 065021
11. Wang B, Zhu S Y. Seismic behavior of self-centering reinforced concrete wall enabled by superelastic shape memory alloy bars. Bulletin of Earthquake Engineering, 2018, 16(1): 479−502
12. Prpov E P, Kasai K, Engelhardt M. Advances in design of eccentrically braced frames. Earthquake Spectra, 1987, 3(1): 43−55
13. Roeder C W, Popov E P. Eccentrically braced steel frames for earthquakes. Journal of the Structural Division, 1978, 104(3): 391−412
14. Popov E P, Engelhardt M D. Seismic eccentrically braced frames. Journal of Constructional Steel Research, 1988, 10(C): 321−354
15. Erochko J, Christopoulos C, Tremblay R, Choi H. Residual drift response of SMRFs and BRB frames in steel buildings designed according to ASCE 7-05. Journal of Structural Engineering, 2011, 137(5): 589−599
16. Xu J, Wu G, Feng D, Fan J J. Probabilistic multi-hazard fragility analysis of RC bridges under earthquake-tsunami sequential events. Engineering Structures, 2021, 238 112250
17. Cao X, Wu G, Feng D C, Wang Z, Cui H R. Research on the seismic retrofitting performance of RC frames using SC-PBSPC BRBF substructures. Earthquake Engineering & Structural Dynamics, 2020, 49(8): 794−816
18. Qiu C X, Zhu S Y. Performance-based seismic design of self-centering steel frames with SMA-based braces. Engineering Structures, 2017, 130: 67−82

19. Berman J W, Bruneau M. Experimental and analytical investigation of tubular links for eccentrically braced frames. Engineering Structures, 2007, 27: 1929−1938
20. Wang B, Nishiyama M, Zhu S, Tani M, Jiang H. Development of novel self-centering steel coupling beams without beam elongation for earthquake resilience. Engineering Structures, 2021, 232: 111827
21. Bin W, Zhu S, Chen K, Huang J. Development of superelastic SMA angles as seismic-resistant self-centering devices. Engineering Structures, 2020, 218: 110836
22. Bertero V, Mahin S A, Herrera R A. A seismic design implications of near fault San Fernando earthquake records. Earthquake Engineering & Structural Dynamics, 1978, 6(1): 31−42
23. Bolt B A. Sesimic input motions for nonlinear structural analysis. ISET Journal of Earthquake Technology, 2004, 41: 223−232
24. Somerville P G, Smith N F, Graves R W, Abrahamson N A. Modification of empirical strong ground motion attenuation relations to include the amplitude and duration effects of rupture directivity. Seismological Research Letters, 1997, 68(1): 199−222
25. Mazza F, Vulcano A. A nonlinear dynamic response of RC framed structures subjected to near-fault fround motions. Bulletin of Earthquake Engineering, 2010, 8(6): 1331−1350
26. Liossatou E, Fardis M. Near-fault effects on residual displacements of RC structures. Earthquake Engineering & Structural Dynamics, 2016, 45(9): 1391−1409
27. Du K, Cheng F, Bai J, Jin S. Seismic performance quantification of buckling-restrained braced RC frame structure under near-fault ground motions. Engineering Structures, 2020, 211: 110447
28. Hu S, Wang W. Seismic design and performance evaluation of low-rise steel buildings with self-centering energy-absorbing dual rocking core systems under far-field and near-fault ground motions. Journal of Constructional Steel Research, 2021, 179: 106545
29. GB 50011–2010. Code for Seismic Design of Buildings. Beijing: Ministry of Housing and Urban-Rural Development of the People's Republic of China, 2010 (in Chinese)
30. Cao X, Feng D, Wu G. Pushover-based probabilistic seismic capacity assessment of RCFs retrofitted with PBSPC BRBF sub-structures. Engineering Structures, 2021, 234: 111919
31. Bruneau M, Chang S E, Eguchi R T, Lee G C, O'rourke T D, Reinhorn A M, Shinozuka M, Tierney K, Wallace W A, von Winterfeldt D. A framework to quantitatively assess and enhance the seismic resilience of communities. Earthquake Spectra, 2003, 19(4): 733−752
32. Cimellaro G P, Reinhorn A M, Bruneau M. Framework for analytical quantification of disaster resilience. Engineering Structures, 2010, 32(11): 3639−3649
33. Cimellaro G P, Reinhorn A M, Bruneau M. Seismic resilience of a hospital system. Structure and Infrastructure Engineering, 2010, 6: 127−144
34. Hazus M H. Multi-Hazard Loss Estimation Methodology-Earthquake Model. Washington, D.C.: Federal Emergency Management Agency, 2003
35. Hu S, Wang W, Qu B. Seismic economic losses in mid-rise steel buildings with conventional and emerging lateral force resisting systems. Engineering Structures, 2020, 204: 110021
36. Xu J, Wu G, Feng D. Near fault ground motion effects on seismic resilience of frame structures damaged in Wenchuan earthquake. Structure and Infrastructure Engineering, 2020, 16(10): 1347−1363
37. Cornell C A, Jalayer F, Hamburger R O, Foutch D A. Probabilistic basis for 2000 SAC federal emergency management agency steel moment frame guidelines. Journal of Structural Engineering, 2002, 128(4): 526−533
38. Chen Zp, Feng Dc, Wu G. Seismic performance and design process majorization of a reinforced concrete grid frame wall. Journal of Earthquake Engineering, 2022, 26(5): 2381−2410
39. Chen Z P, Zhu S, Ma K J, Wu G. Probabilistic seismic capacity analysis of a novel mid-rise large-span cassette structure using multidirectional pushover method. Journal of Earthquake Engineering, 2021, 1−26
40. Ye Zh, Feng D, Wu G. Seismic control of modularized suspended structures with optimal vertical distributions of the secondary structure parameters. Engineering Structures, 2019, 183: 160−179
41. Ye Zh, Shafieezadeh A, Sezen H, Wu G, Feng D C. Cross-level fragility analysis of modularized suspended buildings based on experimentally validated numerical models. Structural Design of Tall and Special Buildings, 2020, 29(14): e1778
42. Chen Z P, Zhu S Y, Ma K J, Wu G, Probabilistic seismic capacity analysis of a novel mid-rise large-span cassette structure using multidirectional pushover method. Journal of Earthquake Engineering, 2021: 199343
43. Qian J, Dong Y. Multi-criteria decision making for seismic intensity measure selection considering uncertainty. Earthquake Engineering & Structural Dynamics, 2020, 49(11): 1095−1114